



Enhancing corrosion resistance in CoCrFeNiTa high entropy alloys via Mo addition

Kang Wang ^a, Yuan Zhu ^a, Peng-wei Wang ^a, Xin Li ^a, Babafemi Malomo ^b, Liang Yang ^{a,*}

^a College of Materials Science and Technology, Nanjing University of Aeronautics and Astronautics, Nanjing 210016, PR China

^b Department of Mechanical Engineering, Obafemi Awolowo University, Ile-Ife, Nigeria

ARTICLE INFO

Keywords:

High-entropy alloys
SEM
Pitting corrosion
EIS

ABSTRACT

In this work, the microstructural characteristics and corrosion resistance of $\text{Co}_{1.5}\text{CrFeNi}_{1.5}\text{Ta}_{0.1}\text{Mo}_x$ ($x = 0, 0.1, 0.3, 0.5$) high entropy alloys (HEAs) fabricated by vacuum arc melting were investigated. To assess the comprehensive corrosion resistance of these alloys in seawater, alkaline or acid rain harsh environments, their electrochemical properties were investigated in solutions of 3.5 wt.% NaCl, 1 M NaOH and 0.5 M H_2SO_4 at room temperature. As minor Mo addition HEA samples indexed a single FCC phase, the precipitation of segregated Ta into the intercellular phase, with increasing Mo additions evolved Ta-rich and Mo-rich growths for the emergence of tuned morphology of Cr- and Mo-rich σ phase in the $\text{Mo}_{0.3}$ and $\text{Mo}_{0.5}$ samples. By potentiodynamic evaluation, $\text{Mo}_{0.3}$ indicated superior corrosion performance with an excellent stability of the passive film in 3.5 wt.% NaCl solution, while the $\text{Mo}_{0.1}$ sample referenced the best passivation behavior in alkaline 1 M NaOH via the probably protective MoO_4^{2-} formation in the outer layer of the film, but in acidic 0.5 M H_2SO_4 , the effect of Mo additions was undermined as the $\text{Mo}_{0.5}$ sample was degraded. Furthermore, the protective passive film was optimally enhanced in the $\text{Mo}_{0.3}$ sample for an excellent brine corrosion resistance in contrast to the Mo_0 sample from localized corrosion and the aggressive degradation of the $\text{Mo}_{0.5}$ sample by preferential corrosion events at the intercellular regions with the σ phase. However, the homogeneously distributed intercellular regions in both $\text{Mo}_{0.1}$ and $\text{Mo}_{0.3}$ characterized the high resistance to pitting exhibited by the HEA alloy in alkaline and seawater environments. Thus, Mo additions could veritably enhance the corrosion resistance of $\text{Co}_{1.5}\text{CrFeNi}_{1.5}\text{Ta}_{0.1}\text{Mo}_x$ HEAs for the development of novel structural alloys with high corrosion performance.

1. Introduction

Evidently, conventional alloys that consist of only a principal element along with a few others in their compositions, such as the iron-, copper-, aluminum or nickel-based traditional alloy systems have been found inadequate in meeting structural performance requirements in aggressive environments [1]. Thus, progressively, high entropy alloys (HEAs) which belong to a class of new and emerging systems constituted by four or more principal elements in equimolar or near-equimolar ratios have now been developed with continued emphasis on structural improvements in extensive scientific studies [2]. Distinctively, HEAs in contrast to the conventional alloys attracted extensive attention because of their unique properties, including excellent mechanical performance, high irradiation resistance, and good corrosion resistance [3–5]. Thus, HEAs are efficiently satisfactory and widely accepted as highly promising candidates for structural material applications.

Over the last decade, a non-equimolar $\text{Co}_{1.5}\text{CrFeNi}_{1.5}$ -based HEA system with the face-centered cubic (FCC) crystal structure was designed, with a 1.5 increase in the constituent molar ratios of Co and Ni to achieve a simple and stable primary phase [6]. In recent times, several variants of $\text{Co}_{1.5}\text{CrFeNi}_{1.5}$ -based HEAs with different addition elements have also been developed. For instance, by the variation of additional Ti/Al ratio, the hardness of the non-equiautomatic $\text{Co}_{1.5}\text{CrFeNi}_{1.5}$ HEAs was significantly enhanced [7]. Interestingly, from a similar perspective, a series of $\text{Al}_x\text{Co}_{1.5}\text{CrFeNi}_{1.5}\text{Ti}_y$ HEAs having much better anti-oxidation properties and resistance to thermal softening as compared with wear resistant steels SUJ2 and SKH51 have also been successfully developed [8]. Reportedly, in pursuant of novel metallic materials with the capacity to effectively resist the influence of acidic and alkaline-contaminated environments, it is known that a $\text{Co}_{1.5}\text{CrFeNi}_{1.5}$ -based HEAs with excellent corrosion resistance in NaCl solution have been developed [9], however to achieve a more comprehensive

* Corresponding author.

E-mail address: yangliang@nuaa.edu.cn (L. Yang).

corrosion resistance of the alloy under extremely aggressive conditions, the influence of doping the HEAs with additional variable elemental compositions comes to light as an intuitive concept, which is yet unexplored and up until now remains an uncharted path of investigation. Fortunately, it is known that elemental Tantalum (Ta) additions in alloys could be advantageous, because the formation of Ta_2O_5 in a passive film can decrease the current density and improve the overall passivation ability for an enhanced corrosion resistance [10–12]. Similarly, by virtue of Molybdenum's (Mo) additions on the corrosion behavior of HEAs in various aqueous environments, FeNiCrMo (P,C,B) bulk metallic glasses indicated superior corrosion resistance in NaCl solution [13], while a decrease in defect density was found within the passive film to enhance the corrosion resistance of $(CoNiV)_{100-x}Mo_x$ HEAs in 0.5 M H_2SO_4 solution [14]. Conversely, however, it was revealed that the corrosion resistance of CoCrFeNiMo_x alloys decreased, owing to the second phases induced by the excessive Mo [15]. Inspired by the aforementioned studies highlighting the corrosion performances of Ta or Mo additions, this current study investigates the conjoint influence of co-additions of Ta and Mo elements on the corrosion resistance and the second phase evolution dynamics of variable Mo, in the HEAs based on the electrochemical behavior of the $Co_{1.5}CrFeNi_{1.5}Ta_{0.1}Mo_x$ HEAs under various aggressive media of NaCl, NaOH and H_2SO_4 solutions that correspondingly denote seawater, alkaline and acidic environments, respectively.

2. Experiments

2.1. Sample preparation

The $Co_{1.5}CrFeNi_{1.5}Ta_{0.1}Mo_x$ ($x = 0, 0.1, 0.3$, and 0.5 in molar ratio) HEAs were prepared by arc melting in a water-cooled copper crucible under a high-purity argon atmosphere. For convenience, these $Co_{1.5}CrFeNi_{1.5}Ta_{0.1}Mo_x$ ($x = 0, 0.1, 0.3$, and 0.5) samples were named; Mo_0 , $Mo_{0.1}$, $Mo_{0.3}$ and $Mo_{0.5}$. Cobalt (Co), Chromium (Cr), Iron (Fe), Nickel (Ni), Tantalum (Ta), and Molybdenum (Mo) with high purities of 99.5% were the raw materials uniformly placed in the crucible according to the weight percents. Table 1 listed the constituent elements of the alloys in weight percentage. Prior to obtaining these multicomponent alloys in the form of $Co_{1.5}CrFeNi_{1.5}Ta_{0.1}Mo_x$, pure titanium (Ti) based alloy materials were firstly melted for 2-times repeatedly by arc melting in order to adsorb the residual air, followed by a 6-times, repeated arc melting of the raw materials to ensure the compositional homogeneity in the ingots which were cast in a water-cooled copper mold with dimensions of $100\text{ mm} \times 10\text{ mm} \times 2\text{ mm}$.

2.2. Structure analysis of the $Co_{1.5}CrFeNi_{1.5}Ta_{0.1}Mo_x$ HEAs

The microstructure and composition analysis of the $Co_{1.5}CrFeNi_{1.5}Ta_{0.1}Mo_x$ ($x = 0, 0.1, 0.3, 0.5$) HEAs were carried out by the scanning electron microscope (SEM, LYRA3 GMU) equipped with an energy dispersive X-ray spectrometry (EDS). The predominant crystalline phases of all samples were identified via X-ray diffraction (XRD) using a Cu K α radiation, and the XRD measurement was set with a diffraction angle (2θ) in the range of 20° to 100° at a speed of $5^\circ/\text{min}$.

Table 1

Stoichiometric compositions in weight ratio (wt.%) of the $Co_{1.5}CrFeNi_{1.5}Ta_{0.1}Mo_x$ ($x = 0, 0.1, 0.3, 0.5$) HEAs.

Designation	Percentage of constituent elements (wt.%)					
	Co	Cr	Fe	Ni	Ta	Mo
Mo_0	29.23	17.20	18.47	29.12	5.98	—
$Mo_{0.1}$	28.34	16.67	17.90	28.22	5.80	3.08
$Mo_{0.3}$	26.69	15.70	16.86	26.59	5.46	8.69
$Mo_{0.5}$	25.23	14.84	15.94	25.13	5.16	13.69

2.3. Electrochemical measurements

To evaluate the comprehensive corrosion resistance of the $Co_{1.5}CrFeNi_{1.5}Ta_{0.1}Mo_x$ HEA samples in various harsh environments, electrochemical measurements were conducted under three environmental conditions: 1 molar concentration (M) sodium hydroxide (NaOH), 0.5 M sulfuric acid (H_2SO_4), and 3.5 wt.% sodium chloride (NaCl) at $25^\circ C$ under atmospheric pressure. The test samples with a size of $10\text{ mm} \times 10\text{ mm} \times 2\text{ mm}$ were mounted in epoxy resin before the electrochemical tests, and the smooth surface area of the samples without protection of epoxy resin was 1 cm^2 . Further to which, all of the samples were cleaned in 99 % ethanol alcohol and distilled water, sequentially ground by 180–2000 grit SiC papers and then polished with a $1\text{ }\mu\text{m}$ diamond paste. The electrochemical station is equipped with a typical three-electrode cell that consists of a saturated calomel electrode (SCE), i.e., an Hg/Hg₂Cl₂ electrode (saturated KCl) having a potential of 0.2412 V higher than the standard hydrogen electrode (SHE), as the reference electrode, and then an experimental sample was the working electrode with a platinum sheet as its counter electrode. Prior to the electrochemical test, the solution was de-aerated by bubbling purified nitrogen gas to remove the interference of dissolved oxygen. The WE-type current wire and CE-type current wire were connected to the working electrode and auxiliary electrode, respectively, while the RE-type potential line was connected to the reference electrode. Prior to the electrochemical test, the solution was de-aerated by bubbling purified nitrogen gas to remove the interference of dissolved oxygen. The Corrtest test application was used for electrochemical testing after the electrochemical station preheated 5 min. The Open Circuit Potential (OCP) was recorded for 1800s to calibrate the experimental sample on a steady state-potential. Subsequently, in the present work, to ensure that the potentiodynamic polarization curves could be completely involved, and based on which several significant parameters could be deduced, potentiodynamic polarization tests were performed from an initial potential of -0.5 V to a final potential of 1 V against the OCP at a scan rate of 1 mV/s over a period of 1500s in 3.5 wt.% NaCl solution, while the text potentials varied from -0.8 to 0.8 V, and from -1.2 V to 0.6 V in 1 M NaOH and 0.5 M H_2SO_4 solutions. Significant electrochemical parameters were determined by fitting the polarization curves: corrosion potential (E_{corr}) [16], corrosion current density (i_{corr}) [16], primary passivation potential (E_{pp}) [17], critical current density (i_{crit}) [17], passivation current density (i_{pass}) [17], breakdown potential (E_b) [18] and the passive region (ΔE) [19]. More importantly, the critical electrochemical impedance spectroscopy (EIS) testing was carried out in the 3.5 wt.% NaCl solution, at the OCP over the operating frequency range of 100 kHz to 10 mHz with a sinusoidal potential amplitude of 10 mV, while maintaining the steady-state potential. To obtain the electrochemical parameters as accurate as possible, the potentiodynamic polarization data in solutions of 3.5 wt.% NaCl, 1 M NaOH, and 0.5 M H_2SO_4 were repeatedly measured for 5 times and finally these electrochemical parameters were determined and listed in Tables 3 and 5, together with the error bars.

2.4. Surface morphology and chemical analysis

The samples were taken out from the epoxy resin, and cleaned with distilled water and anhydrous ethanol after the polarization experiment. The morphology and elemental distributions of the corroded surfaces for all samples were investigated via SEM and EDS measurements.

3. Results and discussion

3.1. Microstructure of the as-cast $Co_{1.5}CrFeNi_{1.5}Ta_{0.1}Mo_x$ HEAs

As the mechanism of Co and Ni elements additions could stimulate the formation of an FCC phase [6], all of the samples were found to exhibit the FCC phase. Specifically, the HEA samples with low Mo additions such as Mo_0 and $Mo_{0.1}$, were indexed as a single FCC phase, in

similarity to the outcomes of a previous work on $\text{Co}_{1.5}\text{CrFeNi}_{1.5}$ HEA [7]. However, as the Mo content increased up to 0.3, a second phase of Cr- and Mo-rich sigma (σ) phase was found to be precipitated on the matrix of FCC phase [9,20,21], as shown in the Fig. 1.

To evaluate the grain size for all samples, the microstructures of Mo_0 , $\text{Mo}_{0.1}$, $\text{Mo}_{0.3}$, and $\text{Mo}_{0.5}$ samples after metallographic etching was shown Fig. 2(a-d). As the Mo content increased, the intercellular phase (brighter phase) for all samples obviously got grown. And 100 grains were randomly selected from each sample, based on which the distribution results were shown in Fig. 2(e-h). The average grain size of Mo_0 , $\text{Mo}_{0.1}$, $\text{Mo}_{0.3}$, and $\text{Mo}_{0.5}$ samples were calculated to be 50.04 μm , 108.79 μm , 144.44 μm , and 216.87 μm , respectively. It is found that the grain size was significantly enlarged with the increase of Mo content. In addition, it was suggested that finer grain size leads to greater grain boundaries, acting as weak spots for preferential corrosion initiation sites [22]. Thus, it is reasonable to find the localized corrosion and a number of large pitting holes of Mo_0 sample after potentiodynamic polarization.

As shown in Fig. 3, the SEM images were composed of a cellular phase (darker phase) as the Region A and an intercellular phase (brighter phase) as the Region B. Region B was observed to grow with an increase of the Mo content, where-in some distinctly noticeable black oxide particles were prominent, due to the fact that the oxygen content in the smelting furnace could not attain an absolute zero around the melting bath [20]. Evidently, according to the EDS data listed in Table 2, it could be inferred that severe segregations of Ta was in effect for its elemental enrichment in Region B. Due to Ta's relatively high melting temperature (T_m), as compared to the T_m values of Fe, Ni, Co and even Mo elements. The solidification of the element into Region B from its naturally segregated state was profound, giving rise to a vigorous Ta-rich intercellular growth that eventually extended into a network-like structure. Accordingly, XRD impressions further indicated that the microstructure remained a fully simple FCC phase in the $\text{Mo}_{0.1}$ sample, to pinpoint that with the addition of Mo content, the morphology of Region B was tuned to achieve a relatively random distribution. On the microstructures of $\text{Mo}_{0.3}$ and $\text{Mo}_{0.5}$ samples illustrated by the images of Fig. 3(c) and (d), it could be stated that apart from the relatively higher melting temperatures of Ta and Mo, their larger atomic sizes and correspondingly slower diffusion rates led to the larger volume fraction of Ta-rich and Mo-rich intercellular growths in $\text{Mo}_{0.3}$ and $\text{Mo}_{0.5}$ samples as compared to that of the $\text{Mo}_{0.1}$ specimen. In congruence with this was the emergence of the σ phase in Region B of $\text{Mo}_{0.3}$ and $\text{Mo}_{0.5}$ samples, and the content of Mo and Cr were mainly elements in the formation of σ phase. This is as a result of Cr and Mo having not only

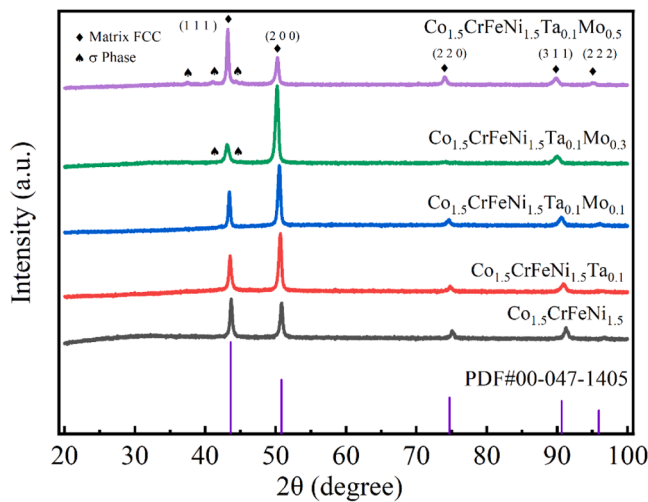


Fig. 1. XRD patterns of $\text{Co}_{1.5}\text{CrFeNi}_{1.5}\text{Ta}_{0.1}\text{Mo}_x$ ($x = 0, 0.1, 0.3, 0.5$), $\text{Co}_{1.5}\text{CrFeNi}_{1.5}$ HEAs and referenced PDF card.

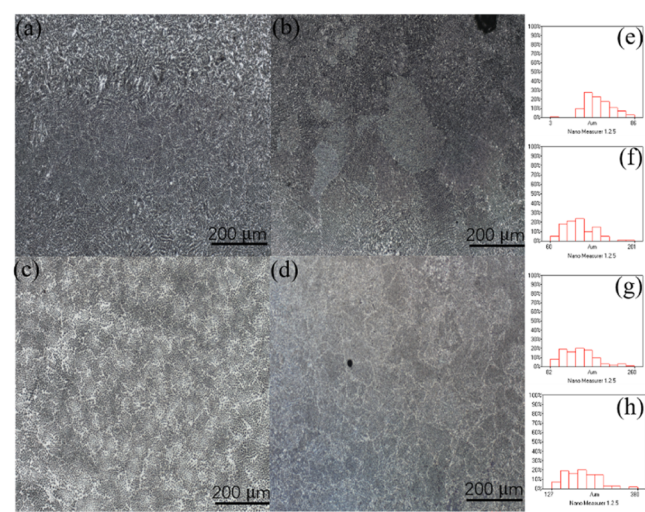


Fig. 2. (a-d) SEM images of the as-cast $\text{Co}_{1.5}\text{CrFeNi}_{1.5}\text{Ta}_{0.1}\text{Mo}_x$ HEAs after metallographic etching; (e-h) The distribution of grain size in all the $\text{Co}_{1.5}\text{CrFeNi}_{1.5}\text{Ta}_{0.1}\text{Mo}_x$ HEA samples, including (a, e) $x = 0$, (b, f) $x = 0.1$, (c, g) $x = 0.3$ and (d, h) $x = 0.5$.

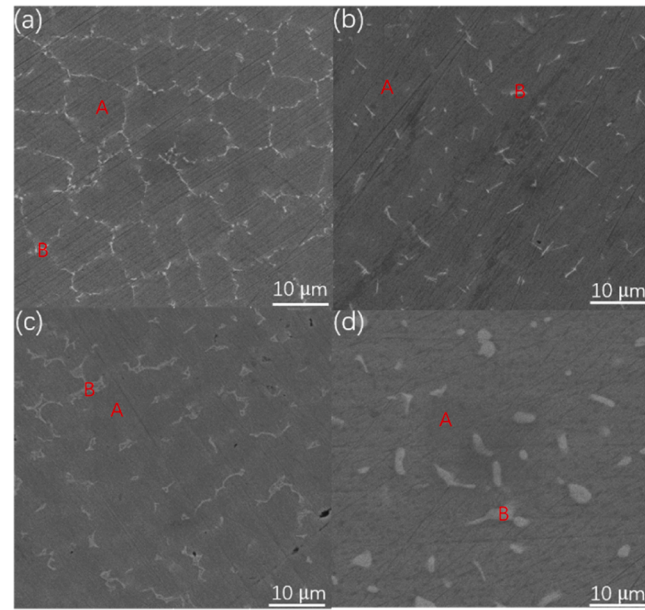


Fig. 3. SEM images of the as-cast $\text{Co}_{1.5}\text{CrFeNi}_{1.5}\text{Ta}_{0.1}\text{Mo}_x$ HEAs, including (a) $x = 0$, (b) $x = 0.1$, (c) $x = 0.3$ and (d) $x = 0.5$, A indicates the cellular phase and the B stands for an intercellular phase.

Table 2

Chemical compositions obtained from EDS analysis of the $\text{Co}_{1.5}\text{CrFeNi}_{1.5}\text{Ta}_{0.1}\text{Mo}_x$ ($x = 0, 0.1, 0.3, 0.5$) HEAs.

Element	Percentage of constituent elements (at.%)					
	Region	Co	Cr	Fe	Ni	Ta
Mo_0	B	23.81	28.21	19.64	20.24	8.10
	A	30.83	18.58	23.42	27.02	0.15
$\text{Mo}_{0.1}$	B	25.39	25.63	20.04	20.08	5.99
	A	30.49	18.27	23.38	25.83	0.03
$\text{Mo}_{0.3}$	B	26.03	25.63	20.07	18.52	3.07
	A	28.18	20.01	21.67	25.07	0.78
$\text{Mo}_{0.5}$	B	24.33	32.16	20.56	13.19	2.99
	A	28.13	20.13	23.15	22.71	0.17

similar electronic configuration but also by the identical BCC crystal structures of their simple substances [23]. Conversely, Co, Fe and Ni elements emerged in Region A due to their similar electronegativities [23].

Furthermore, as the phenomenon of precipitation of the σ phase in HEA samples could be verified by the equivalent chromium content (ECC) equation [24], i.e., ECC = % chromium (Cr) + 0.31 % manganese (Mn) + 1.76 % molybdenum (Mo) + 0.97 % tungsten (W) + 2.02 % vanadium (V) + 1.58 % silicon (Si) + 2.44 % titanium (Ti) + 1.7 % niobium (Nb) + 1.22 % tantalum (Ta) - 0.226 % nickel (Ni) - 0.177 % cobalt (Co) where the formation of the σ phase can be predicated on the ECC value in excess of 17 % [24] it was found in the present study, that the indicated ECC values of the Mo_{0.1}, Mo_{0.3}, and Mo_{0.5} were; 16.64 %, 25.85 %, and 34.07 %, respectively, which evidently confirmed that the σ phase emerged in the Mo_{0.3} and Mo_{0.5} samples.

3.2. Electrochemical properties of the Co_{1.5}CrFeNi_{1.5}Ta_{0.1}Mo_x HEAs

3.2.1. Open circuit potential values

The OCP data for Co_{1.5}CrFeNi_{1.5}Ta_{0.1}Mo_x ($x = 0, 0.1, 0.3$, and 0.5) HEAs was plotted as below. As shown in Fig. 4, several open circuit potential values of the Mo₀, Mo_{0.1}, Mo_{0.3}, and Mo_{0.5} samples were recorded after the oscillation in the OCP curves of the samples got stable. Evidently, the Mo_{0.3} sample with the higher OCP value indicated the better corrosion resistance under 3.5 wt.% NaCl solution. Furthermore, the OCP value of the Mo_{0.1} sample is about -242 mV/SCE, which is higher than those of Mo₀, Mo_{0.3}, and Mo_{0.5} samples, indicating the low activity of Mo_{0.1} sample under 1 M NaOH solution. And under the 0.5 M H₂SO₄ solution, the higher OCP value of Mo₀ sample exhibited the better corrosion resistance than Mo-containing samples.

3.2.2. Potentiodynamic polarization curve under 3.5 wt.% NaCl solution

In as much as the corrosion resistance of Co_{1.5}CrFeNi_{1.5}Ta_{0.1}Mo_x HEAs in various harsh media is pertinent, the performance in saline, seawater remains crucial to extensive applications. Thus, by a further penetrating study, the potentiodynamic polarization curves of the Co_{1.5}CrFeNi_{1.5}Ta_{0.1}Mo_x HEAs in a solution of 3.5 wt.% NaCl were found as illustrated by the plots in Fig. 5. As the Mo content decreased, the corrosion potential of the alloys gradually shifted to the high positive electrode potential, at which the i_{corr} value of Mo_{0.1} and Mo_{0.3} alloys were lower than that of the Mo-free sample as indicated in Table 3. Evidently, the Mo_{0.3} sample indicated a higher positive corrosion potential (E_{corr}) with an associated lower corrosion current density (i_{corr})

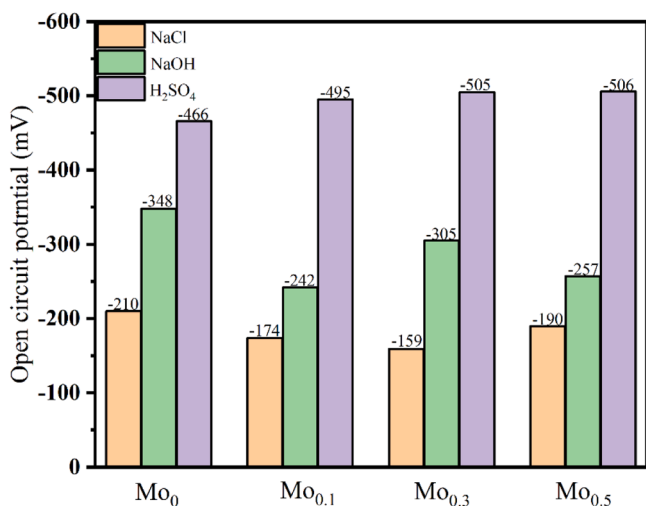


Fig. 4. Open circuit potential (OCP) values of the Co_{1.5}CrFeNi_{1.5}Ta_{0.1}Mo_x ($x = 0, 0.1, 0.3$, and 0.5) HEAs in de-aerated 3.5 wt.% NaCl, 1 M NaOH and 0.5 M H₂SO₄.

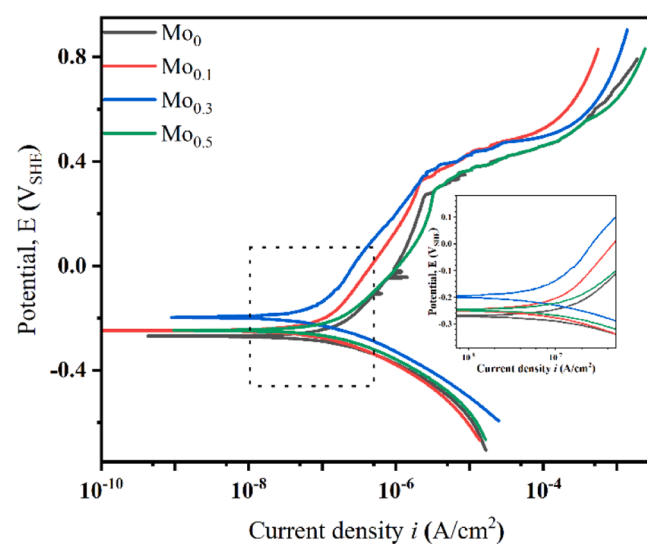


Fig. 5. Potentiodynamic polarization curves of the Co_{1.5}CrFeNi_{1.5}Ta_{0.1}Mo_x ($x = 0, 0.1, 0.3$, and 0.5) HEAs in de-aerated 3.5 wt.% NaCl.

Table 3

Electrochemical parameters of the Co_{1.5}CrFeNi_{1.5}Ta_{0.1}Mo_x ($x = 0, 0.1, 0.3, 0.5$) HEAs in de-aerated 3.5 wt.% NaCl.

Designation	E_{corr} (mV _{SHE})	i_{corr} ($\mu\text{A}/\text{cm}^2$)	E_{pp} (mV _{SHE})	i_{pass} ($\mu\text{A}/\text{cm}^2$)	E_b (mV _{SHE})
Mo ₀	-268 ± 9	0.10 ± 0.004	-187 ± 3	0.26 ± 0.004	272 ± 11
Mo _{0.1}	-243 ± 7	0.07 ± 0.003	-154 ± 4	0.15 ± 0.003	321 ± 4
Mo _{0.3}	-193 ± 5	0.06 ± 0.002	-139 ± 4	0.09 ± 0.003	346 ± 5
Mo _{0.5}	-244 ± 13	0.10 ± 0.008	-179 ± 7	0.22 ± 0.005	285 ± 6

to signify a better corrosion resistance than the other Mo-containing alloys. Furthermore, as the i_{pass} value of Mo_{0.3} sample was also lower than all of the test samples and in particular with an indication of about three-fold reduction relative to that of the Mo₀ sample, it follows that the Mo_{0.3} sample produced a stability of the passive film [25]. According to a previous study [26] where it was revealed that Mo additions could improve the pitting corrosion resistance in a chloride solution, the protective MoO₄²⁻ in the outer regions of the film was cation-selective to effectively inhibit pitting corrosion, causing an accelerated formation of a Cr-oxide inner barrier layer such that the evolving Mo-addition induced double-layer structure produced a stimulation that governed the observed excellent corrosion resistance of Mo_{0.3} sample in NaCl solution.

As Cr and Mo elements can significantly influence the corrosion resistance of HEAs and stainless steels [27], it is required to establish the contributions of their contents. This was accomplished by applying the empirical equation of pitting resistance equivalent (PRE) to draw a correlation between Cr and Mo contents and the pitting phenomenon [27]:

$$\text{PRE} = \% \text{Cr} + 3.3\% \text{Mo} \quad (1)$$

It is found that the PRE values of the corrosion resistance for Mo_{0.1}, Mo_{0.3}, and Mo_{0.5} samples were 25.97, 41.94, and 56.18, respectively, incidentally, the Mo₀ sample indicated the least possible PRE value of 17.2 to imply that pitting corrosion was inhibited by Mo additions according to Eq. (1). Surprisingly, in the Mo_{0.5} sample which indicated the highest the PRE value, corrosion resistance was impeded. Owing to the underlying complex balance between elemental segregations and pitting resistance. Thus, with Mo additions, the intercellular phase of the

samples was characterized by the Cr- and Mo-rich σ phase, while the cellular phase was the Cr- and Mo-depleted phase that undermined the corrosion resistance.

3.2.3. Potentiodynamic polarization curve under 1 M NaOH solution

The corrosion behavior of $\text{Co}_{1.5}\text{CrFeNi}_{1.5}\text{Ta}_{0.1}\text{Mo}_x$ ($x = 0, 0.1, 0.3, 0.5$) HEAs in 1 M NaOH solution is pertinent to the current investigation to expound on the relevance of the HEA in critical alkali-based industrial applications. Here-in, the primary passivation potential (E_{pp}) was found to vary from -322 to -270 mV_{SHE} with the Mo_{0.5} sample indicating the minimal E_{pp} value, as shown in Fig. 6. The electrochemical parameters for the $\text{Co}_{1.5}\text{CrFeNi}_{1.5}\text{Ta}_{0.1}\text{Mo}_x$ ($x = 0, 0.1, 0.3, 0.5$) HEAs were shown in Table 4, from where the Mo_{0.1} sample indicated the least i_{pass} value which not only underscored the best stability of the passive film [25] but also references the slowest dissolution rate of the oxide film in all of the samples [9]. Furthermore, by the minimum value of i_{crit} observed for the Mo_{0.1} sample, it is established that Mo additions positively influenced the passivation behavior of the CoCrFeNiTa HEAs [28]. Upon the determination of the corrosion current density, i_{corr} , from the potentiodynamic polarization curves using the intersection of the anodic and cathodic Tafel lines from -60 to -120 mV for the corrosion potential, the Mo_{0.1} and Mo_{0.5} samples indicated similar values, but the Mo_{0.1} sample indicated the highest peak E_{corr} value. Thus, by Mo additions, the corrosion resistance of the HEAs under 1 M NaOH solution was reasonably enhanced, as established by the Mo_{0.1} sample which indicated the best performance.

Since both the Cr and Mo elements could be unstable at high anodic potential, the phenomenon of trans-passive dissolution in Cr-rich and Mo-rich samples is inevitable, such that the Cr(III) or Mo(IV) is readily oxidized to soluble Cr(VI) or Mo(VI) [9]. By the Cr trans-passivity's higher potential relative to that of the Cr and Mo(VI) it would preferentially emerge in alkaline solutions, which justified the fact that MoO_4^{2-} of the $\text{Co}_{1.5}\text{CrFeNi}_{1.5}\text{Ta}_{0.1}\text{Mo}_x$ ($x = 0, 0.1, 0.3, 0.5$) HEAs was formed in the 1 M NaOH solution. The activity of the protective MoO_4^{2-} in the outer part of the bilayer structure, changed the ionic selectivity of the film to promote the formation of Cr_2O_3 and CrO_3 , which eventually improved the corrosion resistance without altering the film's composition [29]. Thus, it can be inferred that the addition of Mo element in CoCrFeNiTa samples evoked an excellent capacity to prevent localized corrosion in alkaline environments, a result that is consistent with previous investigations [30,31].

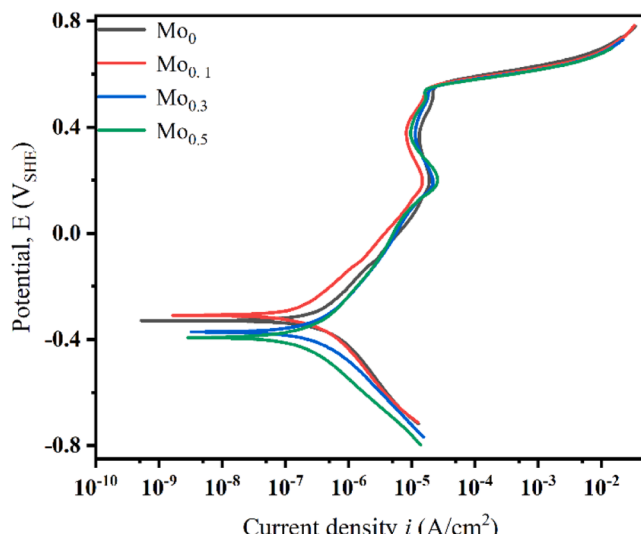


Fig. 6. Potentiodynamic polarization curves of the $\text{Co}_{1.5}\text{CrFeNi}_{1.5}\text{Ta}_{0.1}\text{Mo}_x$ ($x = 0, 0.1, 0.3$, and 0.5) HEAs in de-aerated 1 M NaOH.

Table 4

Electrochemical parameters of the $\text{Co}_{1.5}\text{CrFeNi}_{1.5}\text{Ta}_{0.1}\text{Mo}_x$ ($x = 0, 0.1, 0.3, 0.5$) HEAs in de-aerated 1 M NaOH.

Designation	E_{corr} (mV _{SHE})	I_{corr} ($\mu\text{A}/\text{cm}^2$)	E_{pp} (mV _{SHE})	I_{crit} ($\mu\text{A}/\text{cm}^2$)	i_{pass} ($\mu\text{A}/\text{cm}^2$)	E_b (mV _{SHE})
Mo ₀	-317 ± 8	0.28 ± 0.004	-270 ± 6	0.44 ± 0.003	13.30 ± 0.004	536 ± 7
Mo _{0.1}	-291 ± 6	0.17 ± 0.006	-271 ± 2	0.18 ± 0.002	8.20 ± 0.003	534 ± 6
Mo _{0.3}	-371 ± 9	0.21 ± 0.002	-272 ± 4	0.32 ± 0.003	11.30 ± 0.003	535 ± 9
Mo _{0.5}	-401 ± 11	0.16 ± 0.004	-322 ± 5	0.23 ± 0.002	9.60 ± 0.003	533 ± 11

3.2.4. Potentiodynamic polarization curve under 0.5 M H₂SO₄ solution

The evaluation under this acidic medium, revealed that the alloys yielded a wide passive region ($E_b - E_{\text{pp}} = \Delta E > 1100$ mV), which subsequently diminished with increasing Mo content as evident from the illustrations in Fig. 7, where it is found that the primary passivation potential (E_{pp}) of the Mo₀ sample was lower than that of the Mo-containing samples. Furthermore, with reference to the electrochemical parameters of the $\text{Co}_{1.5}\text{CrFeNi}_{1.5}\text{Ta}_{0.1}\text{Mo}_x$ ($x = 0, 0.1, 0.3, 0.5$) HEAs in the solution of 0.5 M H₂SO₄ as listed the Table 5, it could be stated that the corrosion potential (E_{corr}) of the alloys increased with an increase in Mo content, while the corrosion current density (i_{corr}) values in the Mo₀, Mo_{0.1}, Mo_{0.3}, and Mo_{0.5} samples also increased from 17.4, 20.8, 47.0 to 48.8 $\mu\text{A}/\text{cm}^2$ respectively. In addition, under this condition, the critical current density (i_{crit}) slightly decreased, accompanied by an increase in the passive current density (i_{pass}), a scenario that is consistent with a degraded stability of the passive region. In light of the foregoing, it is confirmed that increasing Mo contents for the $\text{Co}_{1.5}\text{CrFeNi}_{1.5}\text{Ta}_{0.1}\text{Mo}_x$ ($x = 0, 0.1, 0.3, 0.5$) HEA samples, indicated a negative effect on corrosion resistance under 0.5 M H₂SO₄ solution.

Fundamentally, the protective ability of the passive film can be related to its compositions, and it is known that the Cr- or Mo-containing passive film is usually a bilayer structure [32,33], i.e., a coupled outer layer of Cr/Fe oxides and hydroxides with an inner layer of Cr(III) species having a Cr(ox)/Cr(hyd) ratio. In reality, as the Cr content decreases, the smaller $\text{Cr}_2\text{O}_3/\text{Cr}(\text{OH})_3$ partition usually results in a smaller width of the passive film [34]. In addition, it has been revealed that the σ phase in Region B is a Cr- and Mo-rich phase while Region A is a Cr and

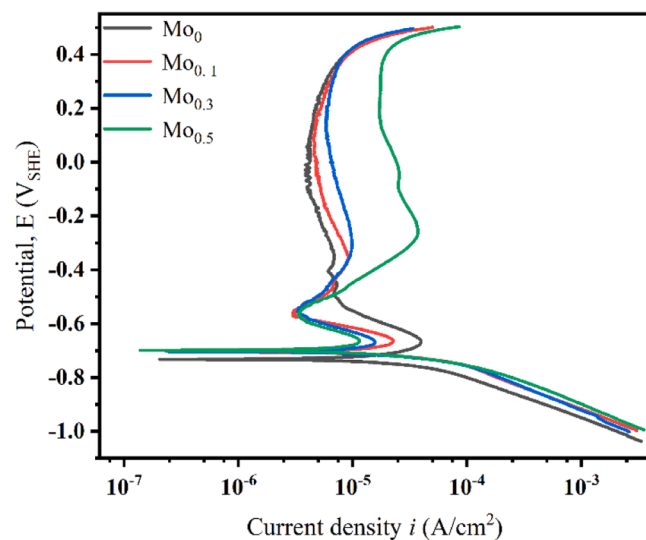


Fig. 7. Potentiodynamic polarization curves of the $\text{Co}_{1.5}\text{CrFeNi}_{1.5}\text{Ta}_{0.1}\text{Mo}_x$ ($x = 0, 0.1, 0.3$, and 0.5) HEAs in de-aerated 0.5 M H₂SO₄.

Table 5Electrochemical parameters of the $\text{Co}_{1.5}\text{CrFeNi}_{1.5}\text{Ta}_{0.1}\text{Mo}_x$ ($x = 0, 0.1, 0.3, 0.5$) HEAs in de-aerated 0.5 M H_2SO_4 .

Designation	E_{corr} (mV _{SHE})	I_{corr} ($\mu\text{A}/\text{cm}^2$)	E_{pp} (mV _{SHE})	I_{crit} ($\mu\text{A}/\text{cm}^2$)	I_{pass} ($\mu\text{A}/\text{cm}^2$)	E_b (mV _{SHE})	ΔE (mV)
Mo_0	-729 \pm 10	17.42 \pm 0.005	-671 \pm 8	39.30 \pm 0.020	3.80 \pm 0.005	362 \pm 8	1033 \pm 10
$\text{Mo}_{0.1}$	-703 \pm 13	20.81 \pm 0.007	-669 \pm 9	22.40 \pm 0.008	4.60 \pm 0.004	353 \pm 5	1022 \pm 11
$\text{Mo}_{0.3}$	-702 \pm 15	47.03 \pm 0.010	-669 \pm 4	15.60 \pm 0.004	5.80 \pm 0.005	348 \pm 9	1017 \pm 8
$\text{Mo}_{0.5}$	-699 \pm 15	48.81 \pm 0.012	-662 \pm 5	11.50 \pm 0.004	17.20 \pm 0.003	349 \pm 4	1011 \pm 13

Mo depleted phase, which not only induced losses in wear resistance and toughness of the Mo-containing steel, but also reduced corrosion resistance by removing Cr and Mo content [35]. In addition, the passive current density (i_{pass}) increased while the i_{crit} value rapidly decreased with increasing Mo, a scenario that is consistent with a previous study [36]. Evidently, the decline in i_{crit} value was an implication of the constraining effect of Mo, orchestrated by its potential to inhibit the active dissolution of Fe and Cr, such that as the Mo content increased from 0 to 0.5 mol, there was a significant growth of Mo interstitial cations in the passive films, by which these cations attained higher oxidation energies relative other interstitial cations. Therefore, the i_{pass} parameter associated with the dissolution of the oxide film, increased due to the passive characteristics of Mo in multi-component samples.

3.3. Analysis of the electrochemical impedance spectroscopy

3.3.1. EIS results under 3.5 wt.% NaCl solution

To further probe the prevailing corrosion reactions in solutions of 3.5 wt.% NaCl, 1 M NaOH, and 0.5 M H_2SO_4 , the Nyquist plot and the Bode plot of the $\text{Co}_{1.5}\text{CrFeNi}_{1.5}\text{Ta}_{0.1}\text{Mo}_x$ ($x = 0, 0.1, 0.3, 0.5$) samples in 3.5 wt.% NaCl solution under OCP condition at the sinusoidal potential amplitude of 10 mV were found as displayed in Fig. 8(a) and (b), the Nyquist plots registered an incomplete semicircle to reasonably suggest that the corrosion event that indicated a sole time constant was governed by the charge transfer process [37]. Thus, the larger the semi-circular radius, the higher the charge transfer resistance and stronger, the protective passive film. From this standpoint in general, minor Mo was found to extend the arc radius while Mo additions in excess reduced it, but essentially, the $\text{Mo}_{0.3}$ sample indicated the largest arc radius, as shown in Fig. 8(a), to underscore an excellent brine corrosion resistance.

It is well-founded that the magnitude of the impedance modulus determines the extent of Cl^- adsorption from the brine solution into the test sample at the low-frequency region of the Bode plot while establishing the corrosion resistance of the alloys in NaCl medium [38]. Hitherto, it can be observed from the Bode plot of Fig. 8(b) on the inference of the Nyquist output that the impedance modulus of the $\text{Mo}_{0.3}$ sample was higher than those of other HEA sample variants at the

low-frequency band, which by implication, underscored the weakest aggression from the corrosive Cl^- medium. However, with the increase of Mo content, the impedance decreased, this along with the decline of phase angle resulted in the increase in capacitance, as evident from the accumulation of charge on the surface of the samples that consequently evoked a decrease in corrosion resistance [39]. Thus, according to the Bode plot, the $\text{Mo}_{0.3}$ sample indicated the largest phase angle, to suggest that a lower charge was amassed for an enhanced corrosion resistance.

3.3.2. EIS results under 1 M NaOH solution

The Nyquist and Bode plots of the Mo_0 , $\text{Mo}_{0.1}$, $\text{Mo}_{0.3}$, and $\text{Mo}_{0.5}$ samples in de-aerated 1 M NaOH under OCP condition were shown Fig. 9. It can be observed in Fig. 9(a) that all samples exhibited the similar features of capacitive semicircles, indicating the similar passive behavior [40,41]. The diameter of the capacitive semicircle was enlarged when the Mo content increased to 0.1, implying that the $\text{Mo}_{0.1}$ sample exhibited the best corrosion resistance, which was consistent with the result of potentiodynamic polarization curves. And it was observed that the $\text{Mo}_{0.1}$ sample had the highest phase angle ($\sim 85^\circ$) at the intermediate frequency regime in Fig. 9(b). Furthermore, the phase angle of $\text{Mo}_{0.1}$ sample was higher than that of Mo_0 , $\text{Mo}_{0.3}$, or $\text{Mo}_{0.5}$ samples in the low-frequency region, implying that the $\text{Mo}_{0.1}$ sample exhibited a lower dissolution rate and a better stability of the passive film [42]. Similarly, the maximum impedance modulus of $\text{Mo}_{0.1}$ sample exhibited the weakest penetration of the corrosive medium through it, which was consistence with the result of Nyquist plot [20].

3.3.3. EIS results under 0.5 M H_2SO_4 solution

Fig. 10(a) showed the Nyquist plots of all the samples in de-aerated 0.5 M H_2SO_4 under OCP condition, in which the arc diameter of the capacitive loops was reduced as the Mo content decreased. Specifically, Mo_0 sample exhibited capacitive loops with larger arc diameters in all samples. As shown in Fig. 10(b), The impedance modulus value of Mo_0 sample was $4.93 \times 10^4 \Omega \cdot \text{cm}^2$ in the low-frequency region, which was larger than that of the $\text{Mo}_{0.1}$ sample ($4.83 \times 10^4 \Omega \cdot \text{cm}^2$). Moreover, the phase angle of Mo_0 sample was -34° , and those of $\text{Mo}_{0.1}$, $\text{Mo}_{0.3}$, and $\text{Mo}_{0.5}$ samples were -30° , -24° , and -20° , respectively. This implies that

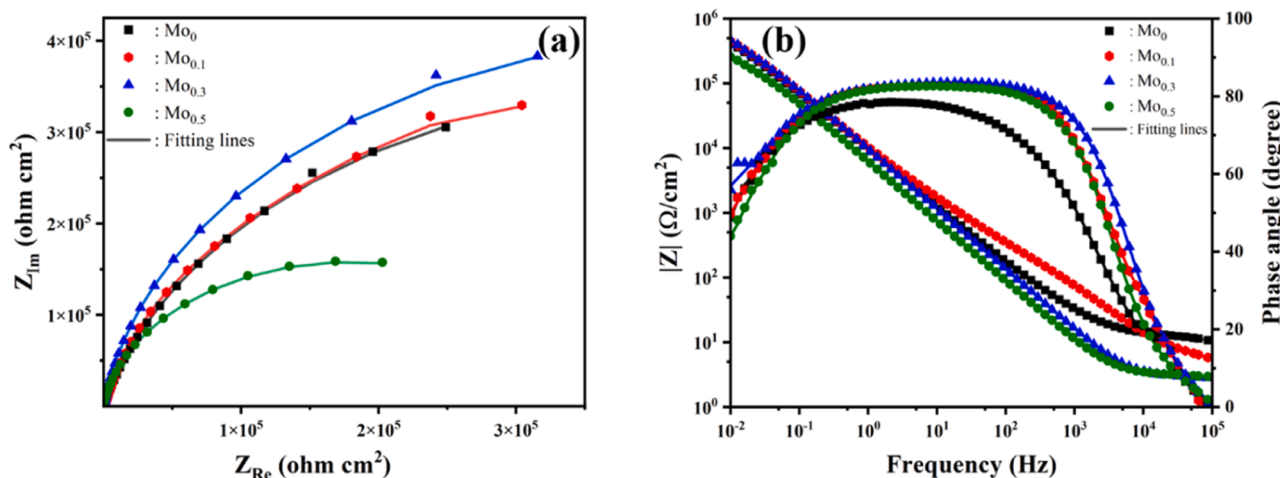


Fig. 8. (a) Nyquist plots and (b) Bode plots of $\text{Co}_{1.5}\text{CrFeNi}_{1.5}\text{Ta}_{0.1}\text{Mo}_x$ ($x = 0, 0.1, 0.3, 0.5$) HEAs in de-aerated 3.5 wt.% NaCl under OCP condition.

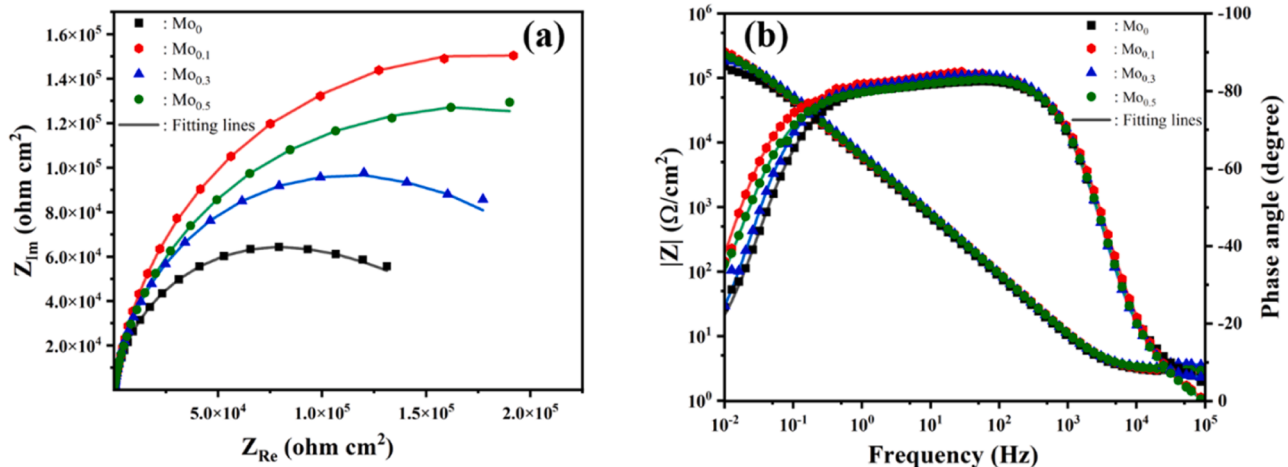


Fig. 9. (a) Nyquist plots and (b) Bode plots of $\text{Co}_{1.5}\text{CrFeNi}_{1.5}\text{Ta}_{0.1}\text{Mo}_x$ ($x = 0, 0.1, 0.3, 0.5$) HEAs in de-aerated 1 M NaOH under OCP condition.

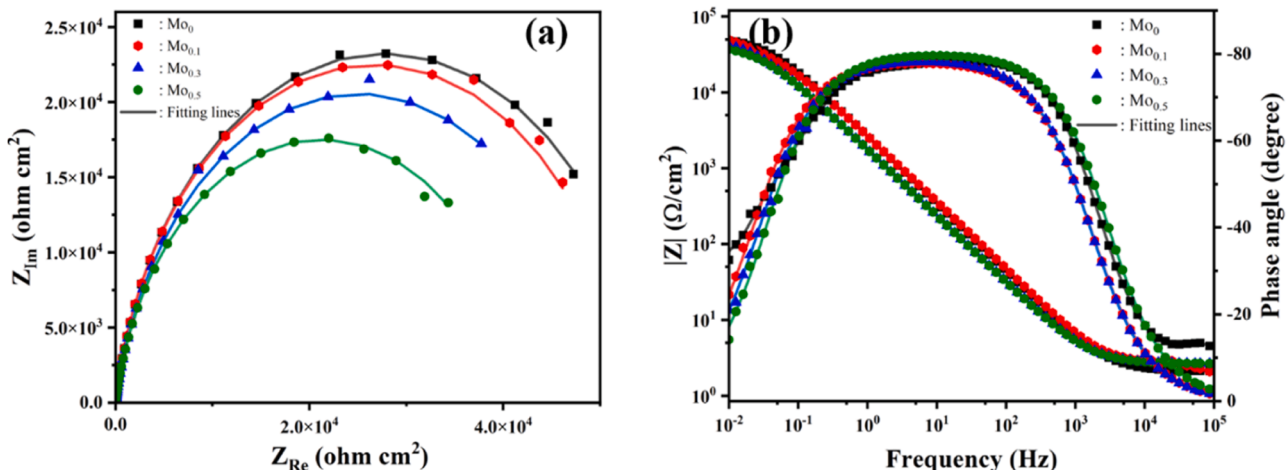


Fig. 10. (a) Nyquist plots and (b) Bode plots of $\text{Co}_{1.5}\text{CrFeNi}_{1.5}\text{Ta}_{0.1}\text{Mo}_x$ ($x = 0, 0.1, 0.3, 0.5$) HEAs in de-aerated 0.5 M H_2SO_4 under OCP condition.

the corrosion resistance decreases with an increase Mo content.

3.3.4. Equivalent electric circuit

Furthermore, to fit the impedance data, it is required that the equivalent electric circuit shown in Fig. 11 as configured by a parallel

connection of the constant phase element (CPE₁) and the polarization resistance (R_2), in series with the solution resistance (R_s) indicates that the true value for the deviation n from a purely capacitive behavior is unequal to unity [43], only then can CPE₁ be adopted to compensate for non-homogeneity instead of a pure capacitor [43]. Table 6 showed the EIS equivalent electric circuit fitting parameters of $\text{Co}_{1.5}\text{CrFeNi}_{1.5}\text{Ta}_{0.1}\text{Mo}_x$ ($x = 0, 0.1, 0.3, 0.5$) HEAs in de-aerated 3.5 wt.% NaCl, 1 M NaOH and 0.5 M H_2SO_4 under OCP conditions.

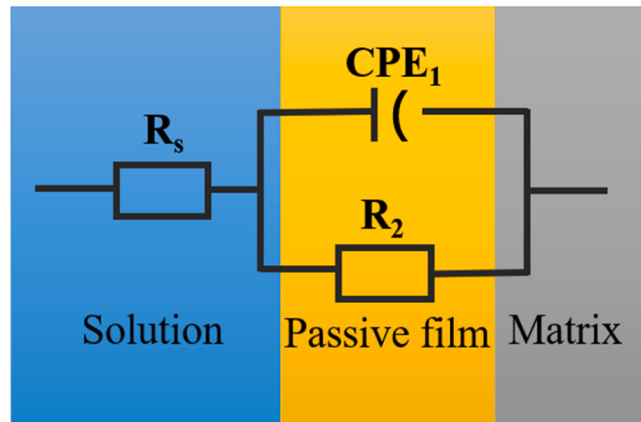


Fig. 11. The equivalent circuit of $\text{Co}_{1.5}\text{CrFeNi}_{1.5}\text{Ta}_{0.1}\text{Mo}_x$ ($x = 0, 0.1, 0.3, 0.5$) HEAs in de-aerated 3.5 wt.% NaCl, 1 M NaOH and 0.5 M H_2SO_4 under OCP condition.

Table 6

Equivalent circuit fitting parameters for EIS of $\text{Co}_{1.5}\text{CrFeNi}_{1.5}\text{Ta}_{0.1}\text{Mo}_x$ ($x = 0, 0.1, 0.3, 0.5$) HEAs in de-aerated 3.5 wt.% NaCl, 1 M NaOH and 0.5 M H_2SO_4 under OCP conditions.

Designation	Solution	R_s ($\Omega \text{ cm}^2$) ± 0.3 %	CPE_1 ($\Omega^{-1} \text{ cm}^{-2} \text{s}^n$) ± 1.2 %	N ± %	R_2 ($\text{k}\Omega \text{ cm}^2$) ± 2.3 %
Mo_0	NaCl	12.36	2.16×10^{-5}	0.86	870.16
	NaOH	2.66	3.28×10^{-5}	0.91	148.89
	H_2SO_4	2.43	7.32×10^{-5}	0.89	59.20
$\text{Mo}_{0.1}$	NaCl	3.02	2.14×10^{-5}	0.90	882.76
	NaOH	2.86	2.68×10^{-5}	0.94	338.00
	H_2SO_4	2.10	8.07×10^{-5}	0.89	53.36
$\text{Mo}_{0.3}$	NaCl	2.83	2.00×10^{-5}	0.93	917.60
	NaOH	3.32	3.09×10^{-5}	0.92	213.17
	H_2SO_4	2.64	11.21×10^{-5}	0.88	50.13
$\text{Mo}_{0.5}$	NaCl	3.02	3.04×10^{-5}	0.91	359.63
	NaOH	2.94	2.99×10^{-5}	0.92	272.08
	H_2SO_4	2.64	11.45×10^{-5}	0.87	42.46

NaOH and 0.5 M H_2SO_4 under OCP conditions, where all of the n values of the CPE_1 were found to be less than 1, indicating the deviation from purely capacitive behavior [44]. By convention, since a large CPE_1 value corresponds to a low density of the passive film [45], it follows that, the largest n value and the least CPE_1 value confirmed that the passive film of the $\text{Mo}_{0.3}$ sample was relatively more stable and protective than those of the other variants to underscore an excellent and superior corrosion resistance, which was remarkably consistent with the results from potentiodynamic polarization in de-aerated 3.5 wt.% NaCl . Furthermore, the R_2 was determined by the interfacial reactions between the solution and passive film [46], and whose value was directly correlated with the corrosion resistance of the sample. From the fitting result of the EIS data in de-aerated 1 M NaOH , the highest R_2 value was obtained in the $\text{Mo}_{0.1}$ sample, implying that the best corrosion resistance was achieved by increasing Mo content to 0.1 at.%. Similarly, the effect of Mo additions was undermined, especially the $\text{Mo}_{0.5}$ sample exhibited the worst corrosion resistance in 0.5 M H_2SO_4 , considering its values of CPE_1 , n , and R_2 .

3.4. Surface morphology of corroded surfaces

3.4.1. Under 3.5 wt.% NaCl solution

To characterize the degree of pitting, the surface topography of the $\text{Co}_{1.5}\text{CrFeNi}_{1.5}\text{Ta}_{0.1}\text{Mo}_x$ HEAs after potentiodynamic polarization in 3.5 wt.% NaCl solution were obtained and shown in Fig. 12. From thence, it could be observed that localized corrosion and a number of large pitting holes were prominent on the Mo_0 sample (Fig. 12(a)), hence this HEA Mo designation cannot provide an effective protection from the passive film. However, it can be observed in Fig. 12(b)–(d) that there was a striking pitting feature around the corrosion region. The maximum corrosion pit depth of Mo_0 , $\text{Mo}_{0.1}$, $\text{Mo}_{0.3}$, and $\text{Mo}_{0.5}$ samples measured by a laser confocal microscope were 3.05 μm , 2.90 μm , 2.76 μm , and 3.55 μm (Fig. 13), respectively. The pit diameters of Mo_0 , $\text{Mo}_{0.1}$, $\text{Mo}_{0.3}$ and $\text{Mo}_{0.5}$ samples were detected to range from 0.5 to 3.0 μm , especially the $\text{Mo}_{0.3}$ and $\text{Mo}_{0.5}$ samples had the smallest value about 0.5 μm . The pitting holes induced by pitting corrosion were preferentially concentrated at the intercellular regions (brighter phase) containing σ phase. In addition, with the addition of Mo, Cr- and Mo-rich σ phase appeared

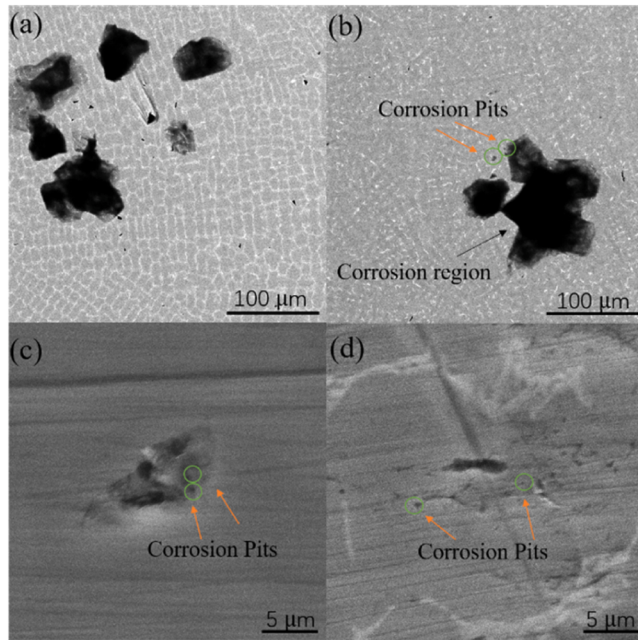


Fig. 12. Surface images of the $\text{Co}_{1.5}\text{CrFeNi}_{1.5}\text{Ta}_{0.1}\text{Mo}_x$ HEAs, including (a) $x = 0$, (b) $x = 0.1$, (c) $x = 0.3$ and (d) $x = 0.5$, after potentiodynamic polarization in de-aerated 3.5 wt.% NaCl .

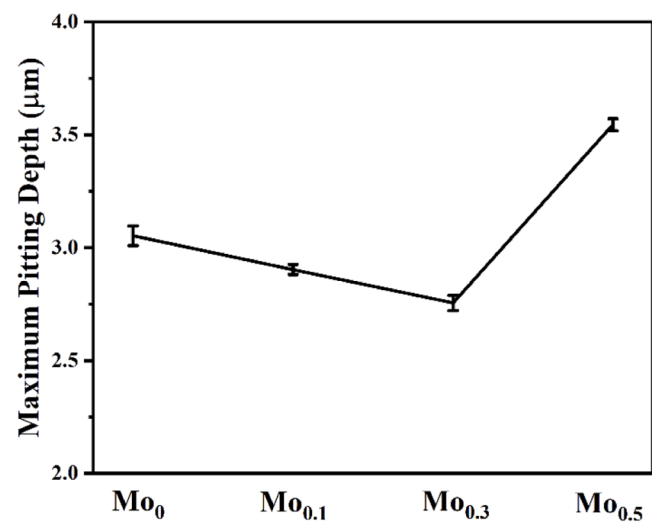


Fig. 13. The maximum pitting depth of $\text{Co}_{1.5}\text{CrFeNi}_{1.5}\text{Ta}_{0.1}\text{Mo}_x$ ($x = 0, 0.1, 0.3, 0.5$) HEAs in de-aerated 3.5 wt.% NaCl .

inside the intercellular region and acted as the cathode, while the cellular region acted as the anode. Therefore, they can compose a micro-galvanic cell, and further promote the formation of pitting holes at the junctions of cellular regions, a result that is consistent with previous investigations [15,21]. By implication, the $\text{Mo}_{0.3}$ sample was the least corroded, given the distinctly fewer and narrower sizes of the corrosion pits relative to those of Mo_0 and $\text{Mo}_{0.1}$ samples, was also in agreement with preceding observations. Furthermore, regarding the $\text{Mo}_{0.5}$ sample, a degraded corrosion resistance was found in correlation with excessive Mo addition. Besides deeper pitting holes, the cracks were observed at the surface of $\text{Mo}_{0.5}$ sample in de-aerated 3.5 wt.% NaCl .

3.4.2. Under 1 M NaOH solution

The surface topographic impressions of $\text{Co}_{1.5}\text{CrFeNi}_{1.5}\text{Ta}_{0.1}\text{Mo}_x$ HEAs after potentiodynamic polarization in de-aerated 1 M NaOH were

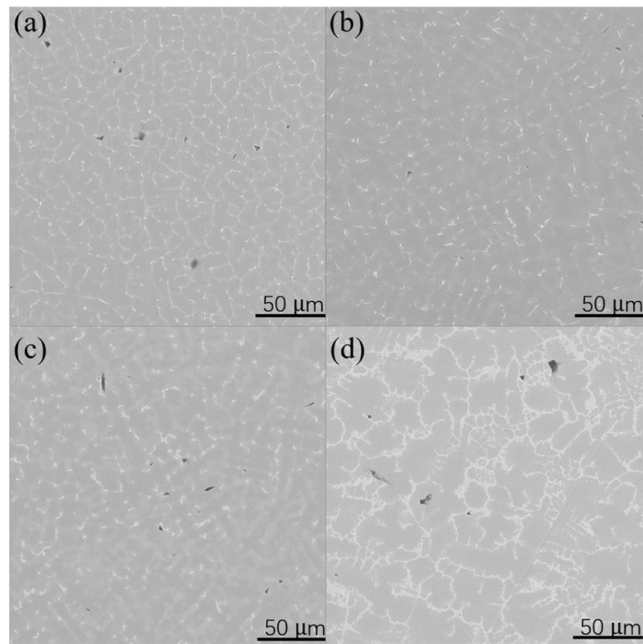


Fig. 14. Surface images of the $\text{Co}_{1.5}\text{CrFeNi}_{1.5}\text{Ta}_{0.1}\text{Mo}_x$ HEAs, including (a) $x = 0$, (b) $x = 0.1$, (c) $x = 0.3$ and (d) $x = 0.5$, after potentiodynamic polarization in de-aerated 1 M NaOH .

captured and presented in Fig. 14. It could be observed that pitting holes associated with NaOH attack mostly occurred at the junctions of the cellular region (darker phase). In Fig. 14(b), the Mo_{0.1} sample indicated the best corrosion resistance by virtue of its fewest number of pitting holes and with a surface being characterized by homogeneously distributed intercellular regions (brighter phase), which is also an observation consistent with the details of potentiodynamic polarization.

3.4.3. Under 0.5 M H₂SO₄ solution

Evidently, apart from the Mo₀ alloy, the surfaces of other Mo-containing samples were found to exhibit various degrees of corrosion as depicted in Fig. 15. According to Table 2, the intercellular region (brighter phase) of Co_{1.5}CrFeNi_{1.5}Ta_{0.1}Mo_x HEAs references a Cr- and Mo-rich region while the cellular region (darker phase), pinpoints to a Cr- and Mo-depleted region. Regardless of the pitting holes, the occurrence of galvanic corrosion at the intercellular regions of Mo_{0.3} and Mo_{0.5} samples, is verifiably in good agreement with a previous work [15], in which the large pitting holes and etch-holes found in the Cr- and Mo-rich regions evidently indicate the progression of corrosion. Thus, the foregoing confirmed that the corrosion resistance of alloys in 0.5 M H₂SO₄ was degraded by the additions of Mo contents.

4. Conclusions

In this present work, the electrochemical characteristics of Co_{1.5}CrFeNi_{1.5}Ta_{0.1}Mo_x ($x = 0, 0.1, 0.3, 0.5$ mol) HEAs in solutions of 3.5 wt.% NaCl, 1 M NaOH and, 0.5 M H₂SO₄, respectively analogous to seawater, alkaline and acidic aggressive media, were investigated to evaluate the corrosion resistance of the alloy. The following conclusions were drawn from the study:

1. The HEA samples with low Mo additions (Mo₀ and Mo_{0.1}) indexed a single FCC phase, but as Mo contents increased, the larger atomic sizes and higher melting temperatures of Ta and Mo forced the solidification of the naturally-segregated Ta into the intercellular phase, stimulating a vigorous Ta-rich and Mo-rich growths that evolved a network-like structure, such that as the morphology was tuned by the homogenous distributions of the intercellular phase, Cr- and Mo-rich σ phase emerged in the Mo_{0.3} and Mo_{0.5} samples.
2. By potentiodynamic evaluation, the Mo_{0.3} sample indicated superior corrosion performance with an excellent stability of the passive film in 3.5 wt.% NaCl solution, while the Mo_{0.1} sample referenced the best passivation behavior in alkaline 1 M NaOH via the MoO₄²⁻ formed in the outer layer of the film stimulated a protective double-layer of Cr (VI) and Mo (VI), but in the acidic 0.5 M H₂SO₄, Mo_{0.5} sample was degraded as the wide passive-region diminished.
3. As the protective passive film was enhanced by minor Mo additions, the Mo_{0.3} sample was confirmed optimal for excellent brine corrosion resistance by the evolution of the constant phase element (CPE₁) in contrast to the Mo₀ sample which suffered the localized corrosion and large pitting holes, and the Mo_{0.5} sample that was degraded by preferential corrosion events at the intercellular regions with the σ phase.
4. The corrosion resistance of the HEA samples in 1 M NaOH medium was highly sensitive to the extremes of Mo additions as degradation of Mo_{0.5} sample was accelerated by the growth of tiny second phases over its extended intercellular region as compared to the homogeneously distributed intercellular regions of the Mo_{0.1} sample which underscored its superior resistance to pitting, and the result of EIS exhibited that the highest R₂ value of Mo_{0.1} sample had the best corrosion resistance in 1 M NaOH solution.

CRedit authorship contribution statement

Kang Wang: Writing – review & editing, Writing – original draft, Methodology, Investigation, Formal analysis, Conceptualization. **Yuan**

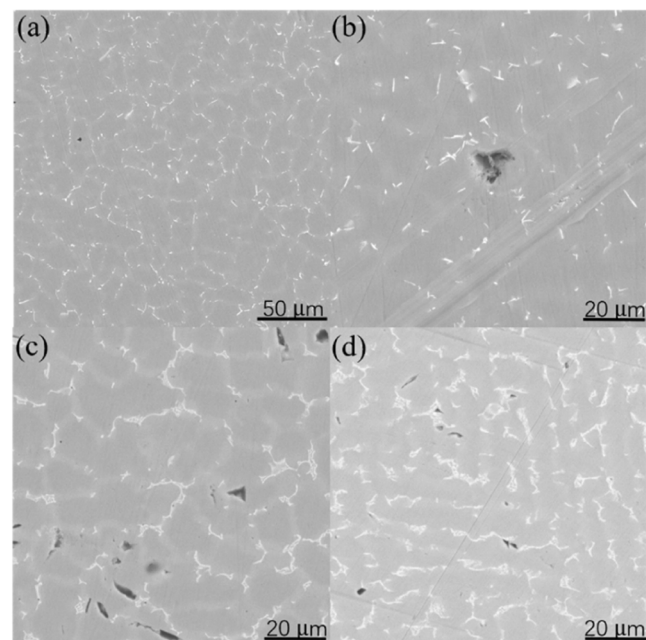


Fig. 15. Surface images of the Co_{1.5}CrFeNi_{1.5}Ta_{0.1}Mo_x HEAs, including (a) $x = 0$, (b) $x = 0.1$, (c) $x = 0.3$ and (d) $x = 0.5$, after potentiodynamic polarization in de-aerated 0.5 M H₂SO₄.

Zhu: Writing – original draft, Validation, Investigation. **Peng-wei Wang:** Resources, Validation, Writing – original draft. **Xin Li:** Formal analysis. **Babafemi Malomo:** Writing – review & editing, Resources, Methodology, Conceptualization. **Liang Yang:** Writing – review & editing, Supervision, Resources, Methodology.

Declaration of competing interest

The authors declare no competing interests.

Data availability

Data will be made available on request.

Acknowledgements

Financial supports from the National Natural Science Foundation of China (Grant No. 51471088) and the Fundamental Research Funds for the Central Universities (Grant No. NS2020043), are gratefully acknowledged.

References

- [1] P. George, D. Raabe, R.O. Ritchie, High-entropy alloys, *Nat. Rev. Mater.* 4 (2019) 515–534.
- [2] J.W. Yeh, S.K. Chen, S.J. Lin, J.Y. Gan, T.S. Chin, T.T. Shun, C.H. Tsau, S.Y. Chang, Nanostructured high-entropy alloys with multiple principal elements: novel alloy design concepts and outcomes, *Adv. Eng. Mater.* 6 (2004) 299–303.
- [3] J.W. Yeh, Recent progress in high-entropy alloys, *Ann. Chim. Sci. Mater.* 31 (2006) 633–648.
- [4] J.W. Yeh, S.J. Lin, T.S. Chin, J.Y. Gan, S.K. Chen, T.T. Shun, C.H. Tsau, S.Y. Chou, Formation of simple crystal structures in Cu-Co-Ni-Cr-Al-Fe-Ti-V alloys with multi-principal metallic elements, *Metall. Mater. Trans. A* 35 (2004) 2533–2536.
- [5] W. Li, P.K. Liaw, Microstructures and properties of high-entropy alloy films and coatings: a review, *Mater. Res. Lett.* 6 (2018) 199–229.
- [6] C.C. Tung, J.W. Yeh, T.T. Shun, S.K. Chen, Y.S. Huang, H.C. Chen, On the elemental effect of AlCoCrCuFeNi high-entropy alloy system, *Mater. Lett.* 61 (2007) 1–5.
- [7] V. Nandal, R. Sarvesha, S.S. Singh, E.W. Huang, Y.J. Chang, A.C. Yeh, J. Jain, S. Neelakantan, Enhanced age hardening effects in FCC based Co_{1.5}CrFeNi_{1.5} high entropy alloys with varying Ti and Al contents, *Materialia* 13 (2020) 100823.

- [8] M.H. Chuang, M.H. Tsai, W.R. Wang, S.J. Lin, J.W. Yeh, Microstructure and wear behavior of $\text{Al}_x\text{Co}_{1.5}\text{CrFeNi}_{1.5}\text{Ti}_y$ high-entropy alloys, *Acta Mater.* 59 (2011) 6308–6317.
- [9] Y.L. Chou, J.W. Yeh, H.C. Shih, The effect of molybdenum on the corrosion behavior of the high-entropy alloys $\text{Co}_{1.5}\text{CrFeNi}_{1.5}\text{Ti}_{0.5}\text{Mo}_x$ in aqueous environments, *Corros. Sci.* 52 (2010) 2571–2581.
- [10] K. Chong, Y. Gao, Z.B. Zhang, Y. Zou, X.B. Liang, Thermal stability and corrosion behavior of a novel $\text{Zr}_{22.5}\text{Ti}_{22.5}\text{Hf}_{22.5}\text{Ni}_{22.5}\text{Ta}_{10}$ high-entropy amorphous alloy, *Corros. Sci.* 213 (2023) 110979.
- [11] Z. Wang, Y. Yan, Y. Wu, X. Huang, Y. Zhang, Y.J. Su, L.J. Qiao, Corrosion and tribocorrosion behavior of equiatomic refractory medium entropy $\text{TiZr}(\text{Hf}, \text{Ta}, \text{Nb})$ alloys in chloride solutions, *Corros. Sci.* 199 (2022) 110166.
- [12] W. Yang, Y. Liu, S.J. Pang, P.K. Liaw, T. Zhang, Bio-corrosion behavior and *in vitro* biocompatibility of equimolar TiZrHfNbTa high-entropy alloy, *Intermetallics* 124 (2020) 106845.
- [13] Y.H. Li, S.W. Wang, X.W. Wang, M.L. Yin, W. Zhang, New FeNiCrMo (P,C,B) high-entropy bulk metallic glasses with unusual thermal stability and corrosion resistance, *J. Mater. Sci. Technol.* 43 (2020) 32–39.
- [14] Z.M. Pan, H. Luo, Q.C. Zhao, H.X. Cheng, X.F. Wang, Y.C. Ma, X.G. Li, Novel Mo-modified medium entropy alloys achieving enhanced corrosion resistance in acidic solution, *Corros. Sci.* 216 (2023) 111094.
- [15] X.L. Shang, Z.J. Wang, Q.F. Wu, J.C. Wang, J.J. Li, J.K. Yu, Effect of Mo addition on corrosion behavior of high-entropy alloys CoCrFeNiMo_x in aqueous environments, *Acta Metall. Sin. Engl.* 32 (2019) 41–51.
- [16] A. Dhawan, S. Roychowdhury, P.K. De, S.K. Sharma, Potentiodynamic polarization studies on bulk amorphous alloys and $\text{Zr}_{46.75}\text{Ti}_{8.25}\text{Cu}_{7.5}\text{Ni}_{10}\text{Be}_{27.5}$ and $\text{Zr}_{65}\text{Cu}_{17.5}\text{Ni}_{10}\text{Al}_{7.5}$, *J. Non Cryst. Solids* 351 (2005) 951–955.
- [17] M.A. Ameri, A.M. Fekry, F. El-Taib Heikal, Electrochemical behaviour of passive films on molybdenum-containing austenitic stainless steels in aqueous solutions, *Electrochim. Acta* 50 (2004) 43–49.
- [18] M.L. Morrison, R.A. Buchanan, A. Peker, W.H. Peter, J.A. Horton, P.K. Liaw, Cyclic-anodic-polarization studies of a $\text{Zr}_{41.2}\text{Ti}_{13.8}\text{Ni}_{10}\text{Cu}_{12.5}\text{Be}_{22.5}$ bulk metallic glass, *Intermetallics* 12 (2004) 1177–1181.
- [19] C.P. Lee, Y.Y. Chen, C.Y. Hsu, J.W. Yeh, H.C. Shih, The effect of boron on the corrosion resistance of the high entropy alloys $\text{Al}_{0.5}\text{CoCrCuFeNiB}_x$, *J. Electrochem. Soc.* 154 (2007) C424–C430.
- [20] J.K. Wang, Y.S. Chen, Y.H. Zhang, Y.C. Zhang, J.J. Li, J. Liu, Y. Liu, W.Z. Li, Microstructure evolution and acid corrosion behavior of $\text{CoCrFeNiCu}_{1-x}\text{Mo}_x$ high-entropy alloy coatings fabricated by coaxial direct laser deposition, *Corros. Sci.* 198 (2022) 110108.
- [21] Y. Fu, C. Huang, C.W. Du, J. Li, C.D. Dai, H. Luo, Z.Y. Liu, X.G. Li, Evolution in microstructure, wear, corrosion, and tribocorrosion behavior of Mo-containing high-entropy alloy coatings fabricated by laser cladding, *Corros. Sci.* 191 (2021) 109727.
- [22] A.A. Rodriguez, J.H. Tylczak, M.C. Gao, P.D. Jablonski, M. Detrois, M. Ziomek-Moroz, J.A. Hawk, Effect of Molybdenum on the corrosion behavior of High-entropy alloys CoCrFeNi_2 and $\text{CoCrFeNi}_2\text{Mo}_{0.25}$ under sodium chloride aqueous conditions, *Adv. Mater. Sci. Eng.* 2018 (2018) 3016304.
- [23] T.T. Shun, L.Y. Chang, M.H. Shiu, Microstructure and mechanical properties of multiprincipal component CoCrFeNiMo_x alloys, *Mater. Charact.* 70 (2012) 63–67.
- [24] O. Conejero, M. Palacios, S. Rivera, Premature corrosion failure of a 316L stainless steel plate due to the presence of sigma phase, *Eng. Fail. Anal.* 16 (2009) 699–704.
- [25] D. Bi, Y. Chang, H. Luo, Z.M. Pan, Q.C. Zhao, H.X. Cheng, X.F. Wang, C.Y. Qiao, Z. Q. Ni, A.Y. Liu, Corrosion behavior and passive film characteristics of AlNbTiZrSi_x high-entropy alloys in simulated seawater environment, *Corros. Sci.* 224 (2023) 111530.
- [26] C.R. Clayton, Y.C. Lu, A bipolar model of the passivity of stainless steel: the role of Mo addition, *J. Electrochem. Soc.* 133 (1986) 2465–2473.
- [27] J.W. Simmons, Overview: high-nitrogen alloying of stainless steels, *Mater. Sci. Eng. A* 207 (1996) 159–169.
- [28] Q.K. Zhang, N. Lin, He Y.H., Effects of Mo additions on the corrosion behavior of WC-TiC-Ni hardmetals in acidic solutions, *Int. J. Refract. Met. Hard Mater.* 38 (2013) 15–25.
- [29] C.M. Abreu, M.J. Cristóbal, R. Losada, X.R. Núvoa, G. Pena, M.C. Pérez, Comparative study of passive films of different stainless steels developed on alkaline medium, *Electrochim. Acta* 49 (2004) 3049–3056.
- [30] X.W. Yuan, W.T. Li, X. Wang, H.Y. Yang, Mo effect on natural passivation and corrosion behavior of duplex stainless steels in alkaline media, *J. Electrochem. Soc.* 167 (2020) 161509.
- [31] S.D. Guo, R. Bao, S.Y. Li, Y.W. Ye, E.T. Zhu, W.J. Wang, Y.X. Zhang, H. Chen, Y. Ye, The role of Y_2O_3 , Cu, Mo and Mo_2C additives on optimizing the corrosion resistance of WC-6Co cemented carbide in HCl and NaOH solutions, *J. Alloy. Compd.* 827 (2020) 154269.
- [32] V. Maurice, H. Peng, L.H. Klein, A. Seyeux, S. Zanna, P. Marcus, Effects of molybdenum on the composition and nanoscale morphology of passivated austenitic stainless steel surfaces, *Faraday Discuss.* 180 (2015) 151–170.
- [33] E. De Vito, P. Marcus, XPS study of passive films formed on molybdenum-implanted austenitic stainless steels, *Surf. Interface Anal.* 19 (1992) 403–408.
- [34] C.D. Dai, H. Luo, J. Li, C.W. Du, Z.Y. Liu, J.Z. Yao, X-ray photoelectron spectroscopy and electrochemical investigation of the passive behavior of high-entropy FeCoCrNiMo_x alloys in sulfuric acid, *Appl. Surf. Sci.* 499 (2020) 143903.
- [35] O. Conejero, M. Palacios, S. Rivera, Premature corrosion failure of a 316L stainless steel plate due to the presence of sigma phase, *Eng. Fail. Anal.* 16 (2009) 699–704.
- [36] P. Schmutz, D. Landolt, In-situ microgravimetric studies of passive alloys: potential sweep and potential step experiments with Fe-25Cr and Fe-17Cr-33Mo in acid and alkaline solution, *Corros. Sci.* 41 (1999) 2143–2163.
- [37] N. Kumar, M. Fusco, M. Komarasamy, R.S. Mishra, M. Bourham, K.L. Murty, Understanding effect of 3.5wt.% NaCl on the corrosion of $\text{Al}_{0.1}\text{CoCrFeNi}$ high-entropy alloy, *J. Nucl. Mater.* 495 (2017) 154–163.
- [38] C.A. Della Rovere, J.H. Alano, R. Silva, P.A.P. Nascente, J. Otubo, S.E. Kuri, Characterization of passive films on shape memory stainless steels, *Corros. Sci.* 57 (2012) 154–161.
- [39] S.L.D. Assis, S. Wolynec, I. Costa, Corrosion characterization of titanium alloys by electrochemical techniques, *Electrochim. Acta* 51 (2006) 1815–1819.
- [40] H. Luo, S.J. Gao, C.F. Dong, X.G. Li, Characterization of electrochemical and passive behaviour of alloy 59 in acid solution, *Electrochim. Acta* 135 (2014) 412–419.
- [41] C. Ai, F. He, M. Guo, J. Zhou, Z.J. Wang, Z.W. Yuan, Y.J. Liu, L. Liu, Alloy design, micromechanical and macromechanical properties of CoCrFeNiTa_x eutectic high entropy alloys, *J. Alloy. Compd.* 735 (2018) 2653–2662.
- [42] K.J. Lu, Z.R. Lei, S. Deng, J.H. Li, T.F. Feng, Z.Y. Luo, X.K. Ma, Synergistic effects of grain sizes on the corrosion behavior and mechanical properties in a metastable high-entropy alloy, *Corros. Sci.* 225 (2023) 111588.
- [43] M. BenSalah, R. Sabot, E. Triki, L. Dhouibi, P. Refait, M. Jeannin, Passivity of sanicro28 (UNS N-08028) stainless steel in polluted phosphoric acid at different temperatures studied by electrochemical impedance spectroscopy and Mott-Schottky analysis, *Corros. Sci.* 86 (2014) 61–70.
- [44] H. Luo, S.W. Zou, Y.H. Chen, Z.M. Li, C.W. Du, X.G. Li, Influence of carbon on the corrosion behavior of interstitial equiatomic CoCrFeMnNi high-entropy alloys in a chlorinated concrete solution, *Corros. Sci.* 163 (2020) 108287.
- [45] M. Kissi, M. Bouklah, B. Hammouti, M. Benkaddour, Establishment of equivalent circuits from electrochemical impedance spectroscopy study of corrosion inhibition of steel by pyrazine in sulphuric acidic solution, *Appl. Surf. Sci.* 252 (2006) 4190–4197.
- [46] Y. Qiu, S. Thomas, M.A. Gibson, H.L. Fraser, K. Pohl, N. Birbilis, Microstructure and corrosion properties of the low-density single-phase compositionally complex alloy AITIVCr, *Corros. Sci.* 133 (2018) 386–396.